Tanaka et al. Earth, Planets and Space (2025) 77:32
https://doi.org/10.1186/s40623-025-02153-5

Earth, Planets and Space

FULL PAPER

Open Access

A possibility of fluid migration due to the 2023 M6.5 Noto Peninsula earthquake suggested from precise gravity measurements

Yoshiyuki Tanaka[1*], Ryuichi Nishiyama[2], Akito Araya[2], Hiromu Sakaue[1], Kazuma Nakakoji[1], Taisei Takata[1,3], Takuya Nishimura[4], Yoshihiro Hiramatsu[5] and Akihiro Sawada[5]

Abstract

The Noto Peninsula has experienced seismic swarms accompanied by transient crustal deformation since November 2020, followed by two major earthquakes (M6.5 on May 5, 2023, and M7.6 on Jan. 1, 2024). Previous studies have suggested that fluids are involved in a series of activities. Most evidence on fluids constrains only their existence, and quantitative information on dynamic fluid migration remains scarce. Past precise gravity measurements in volcanic areas captured changes at the µGal scale (10^{-8} m/s^2) due to magma movement. Here, we report the gravity difference caused by the M6.5 earthquake that was obtained via a similar method of measurement. Most of the observed gravity change can be explained by a fault slip model determined from the geodetic inversion of GNSS data. However, a significant change of approximately 10 µGal remains unexplainable in the northern coastal area of the northeastern tip of the Noto Peninsula. To explain this change, we estimate environmental effects, such as groundwater and sea-level variations. These environmental effects are too small to fully explain the change unless large local groundwater changes that are not represented in the groundwater model are considered. Instead, adding a fluid-fed fault that opens above the coseismic fault could reasonably explain both the GNSS and gravity data. The inferred volume of fluids is approximately 10% of the volume to have accumulated in a deeper fault by June 2022, as estimated from GNSS data. This result suggests that fluids migrating to shallower areas may have increased the risk of the M7.6 earthquake. The relatively shallow seismic velocity anomalies inferred by seismic tomography might indicate that such an upward migration process due to large earthquakes has been repeated in the past.

Keywords Noto Peninsula, Earthquake, Seismic swarm, Crustal deformation, Fluid, Gravity, GNSS, Absolute gravimeter

*Correspondence:
Yoshiyuki Tanaka
y-tanaka@eps.s.u-tokyo.ac.jp
Full list of author information is available at the end of the article

© The Author(s) 2025. **Open Access** This article is licensed under a Creative Commons Attribution 4.0 International License, which permits use, sharing, adaptation, distribution and reproduction in any medium or format, as long as you give appropriate credit to the original author(s) and the source, provide a link to the Creative Commons licence, and indicate if changes were made. The images or other third party material in this article are included in the article's Creative Commons licence, unless indicated otherwise in a credit line to the material. If material is not included in the article's Creative Commons licence and your intended use is not permitted by statutory regulation or exceeds the permitted use, you will need to obtain permission directly from the copyright holder. To view a copy of this licence, visit http://creativecommons.org/licenses/by/4.0/.

Graphical Abstract

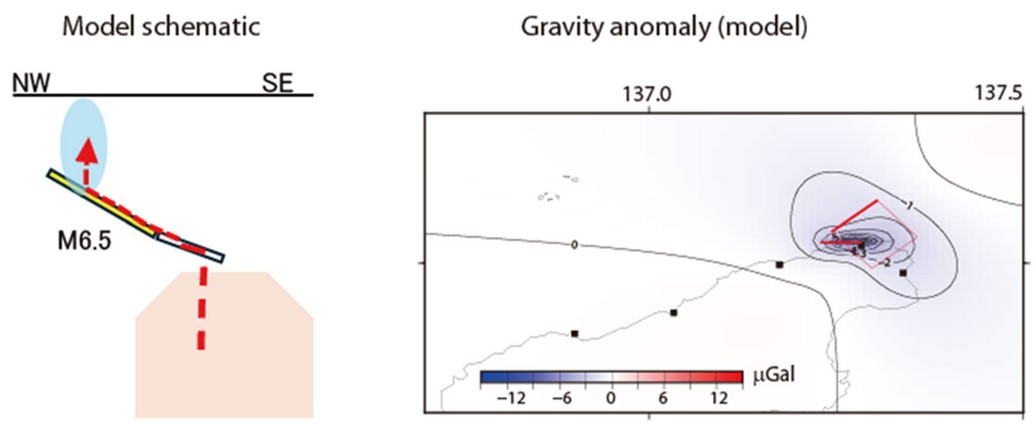

1 Introduction

The Noto Peninsula is located on the back-arc side of the Japanese island arc, where the Pacific Plate (PA) and the Philippine Sea Plate (PHS) subduct beneath the Eurasian Plate (EU) (Fig. 1). The recent tectonics of the northern Noto Peninsula are characterized mainly by offshore active reverse faults under northwest-southeast compression, which occasionally caused the occurrence of large earthquakes such as the 2007 M6.9 Noto Peninsula earthquake, and the absence of volcanic activity (Sato 1994; Yamada and Takahashi 2021; Nakajima 2022). Since November 2020, an earthquake swarm has been active at

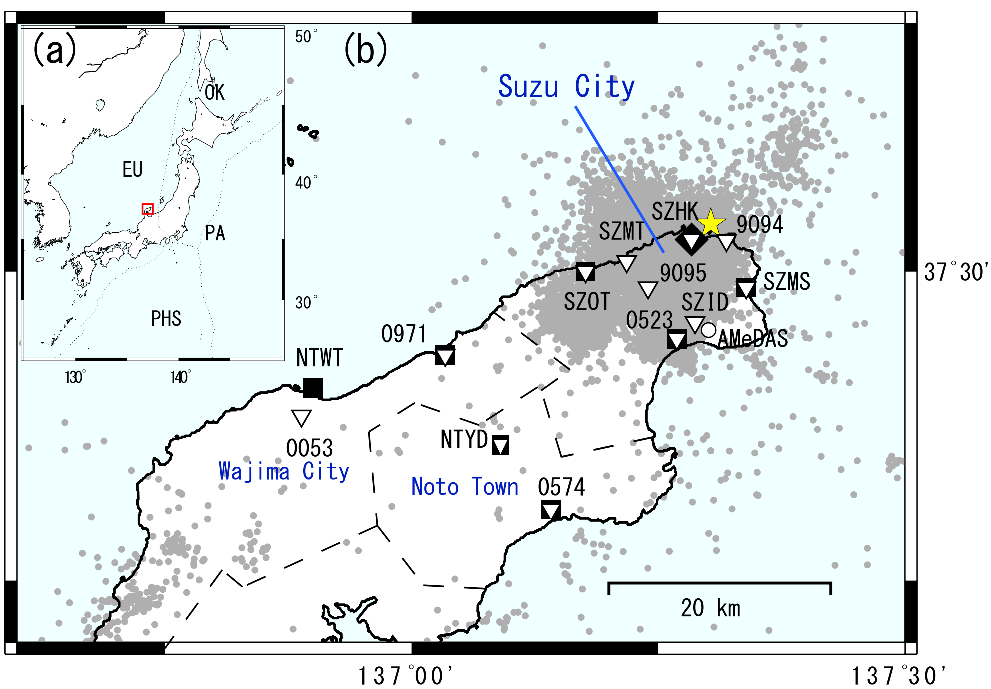

Fig. 1 Study area. **a** Tectonic setting. The area shown by the red box is magnified to **b**. **b** Observation sites. The black diamond (SZHK) and squares denote the absolute and relative gravity measurement sites, respectively, and the inverted triangles represent the GNSS stations used in this study. The gray dots represent the epicenters of earthquakes from December 2020 to March 2023. The star denotes the epicenter of the M6.5 event on May 5, 2023. The white circle marked by AMeDAS represents the AMeDAS station. Suzu city and Wajima city are located at the northeastern and western ends of the northern Noto Peninsula, respectively. The dashed lines represent the boundary lines of the local governments

a depth of approximately 16 km in the southern part of Suzu city (Fig. 1), accompanied by gradual crustal uplift, and the earthquake swarm has propagated counterclockwise as its sources have become slightly shallower over 2.5 years (Yoshida et al. 2023). M6.5 and M7.6 earthquakes occurred consecutively in the northern coastal areas on May 5, 2023, and January 1, 2024, respectively.

The above seismic activity since November 2020 is considered to have been caused by crustal fluids. Many studies, including seismic and electromagnetic observations (e.g., Nakajima and Hasegawa 2007; Nakajima 2022; Matsubara et al. 2022; Yoshimura et al. 2023; Okada et al. 2024) and geochemical analyses (e.g., Nakamura et al. 2008; Umeda et al. 2009), suggest that fluids supplied by the underlying oceanic plate(s) have risen close to earthquake sources.

Compared with such evidence for the "static" fluid distribution in the present era that is formed by the accumulation of past fluid flows, there is little evidence to suggest that the dynamic and transient fluid flows occurred during the earthquake swarm and major earthquakes. Nishimura et al. (2023) analyzed Global Navigation Satellite System (GNSS) crustal deformation data up to the 2023 M6.5 earthquake and reported that between November 2020 and June 2022, a volume of approximately 3×10^7 m^3 of fluid was supplied into a southeast-dipping fault from a deeper region. Yoshida et al. (2023) noted that upward fluid migration indicated by the gradual shallowing of the sources of the earthquake swarm triggered the 2023 M6.5 earthquake. Kato (2024) noted that the fast propagation velocity of the front of the aftershock of the 2023 M6.5 earthquake suggested that the coseismic rupture increased permeability and caused the upwelling of fluids.

Crustal deformation data can be used to quantitatively estimate the volume of material that moves in a volcanic region on the basis of elastic deformation models (e.g., the Mogi model). However, such data for geometrical deformation cannot reveal which material (magma/water/gas) is truely involved. To overcome this problem, gravity observations which sense mass movement can be combined. Previous studies using absolute gravimeters have successfully captured gravity changes on the order of only 1 μGal (10^{-8} m/s^2) associated with volcanic activity (e.g., Yoshida et al. 1999; Okubo 2020) and subsurface mass movement in a slow slip area that might be associated with crustal fluid flow (Tanaka et al. 2018).

The purpose of this study is to obtain quantitative information on transient fluid flow in the Noto Peninsula on the basis of gravity observations. This study focuses on the gravity changes caused by the May 2023 M6.5 earthquake. "Data and methods" section describes the gravity observations and the methods used to evaluate the obtained data. "Results" section presents the observed results, groundwater variation as a major error source, and gravity changes due to coseismic fault slip as known causes. "Discussion" section discusses possible causes of residual unexplainable gravity anomalies, including fluid migration. Finally, "Conclusions" section summarizes the results.

2 Data and methods

2.1 Gravity data

Campaign observations were carried out on March 7–9, May 16–17 and September 6–7 in 2023 via an FG5 absolute gravimeter #212 and Lacoste-Romberg G-type relative gravimeters #581 and #705. Details of the observations with these instruments and the data processing are described in Okubo et al. (1997) and Tanaka et al. (2010). Figure 1b shows the sites at which gravity measurements were taken. Absolute gravity measurements were made in an air-conditioned room on the ground floor of a building originally used as an elementary school (SZHK in Fig. 1b). At each campaign, at least 25 hours of continuous absolute gravity data were obtained. The gravity differences from SZHK to the other sites were measured using relative gravimeters. All the gravity measurement sites were in the vicinity of continuous GNSS stations (Nishimura et al. 2023).

The absolute gravity data were processed as follows. The set gravity data (100 drops/set, set interval = 30 min) were corrected for solid-Earth and ocean tides with TIDE4N (Tamura et al. 1991) and GOTIC2 (Mastumoto et al. 2001). The effects of atmospheric pressure and polar motion were removed, using an admittance of −0.3 μGal/hPa and the Earth orientation parameters published in Bulletin B of the International Earth Rotation Service (https://datacenter.iers.org/eop.php). Throughout the three campaigns, the laser 1F voltage was stable and the correction for atmospheric pressure changes was within 2 μGal.

Figure 2 shows the residual absolute gravity data obtained after these corrections. In March (left panel), we obtained 50-h (i.e., 100 sets) continuous data. A weighted average of these sets, which is based on the standard deviations (SDs) for the set gravity values, was used to calculate the final gravity value (980,001,210 μGal) and the measurement error (0.25 μGal). The instrumental and model uncertainties estimated by the FG5 software were added, and the total uncertainty became approximately 2 μGal. The results were within 1 μGal when different 25-hour successive data were used for the 50-hour dataset. In May (middle panel), during DOYs (days of year) 137.0–137.4, the south-southwest wind speed increased and the set SDs increased to 2–3 times higher than those before DOY 137.0. Beginning

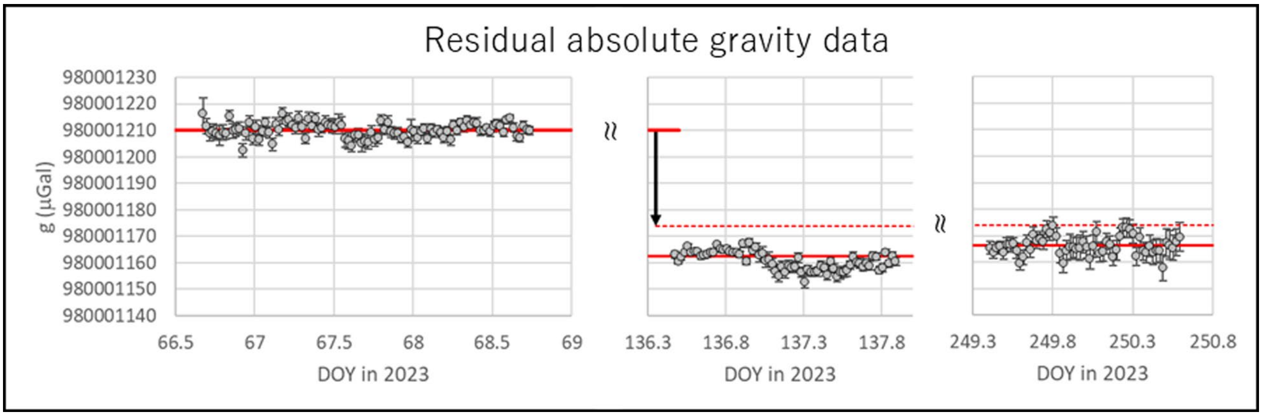

Fig. 2 Absolute gravity data at SZHK after the corrections. The horizontal axis denotes the day of the year. The vertical axis represents the absolute gravity value, and each data point shows a set gravity value, consisting of approximately 100 drops (a few outliers can be rejected) and the set interval is 30 min. The horizontal red solid line in each panel shows the final gravity values calculated with the 25- or 50-h data (see text). The uncertainty of the final values is approximately 2 µGal. The horizontal broken line denotes the value expected from the observed coseismic vertical displacement ("A "dynamic" gravity anomaly" section). The gap between the solid and broken lines in the middle panel represents the negative gravity anomaly

on DOY ~ 137.0, gravity gradually decreased and then recovered to approximately the same level. To reduce tidal effects that cannot be fully expressed by the above tidal models, a weighted average of the first 25 hours of data was used to calculate the final gravity value (980,001,163 ± 0.4 µGal). The total uncertainty was estimated to be approximately 2 µGal, as it was in March. For comparison, the results when the first and last 13-hour data were used were 980,001,164 ± 0.3 µGal and 98,001,160 ± 0.5 µGal, respectively. In September (right panel), we obtained approximately 36 hours of continuous data. A weighted average of the first 25-hour data when the set SDs were smaller was used to calculate the final value (980,001,166 ± 0.5 µGal). The total uncertainty was again approximately 2 µGal.

The relative gravity data were processed according to Tanaka et al. (2010). The difference between the daily round-trip measurements after tidal effects were removed for each gravimeter was smaller than 10 µGal in almost all of the cases. We did not use the data obtained at 0523, NTYD and 0574 in the following analysis because the differences between March and May were 40–90 µGal even though the results from the two gravimeters agreed within 10–20 µGal, implying that local disturbances were too strong to detect tectonic movements. For uncertainty, even if the round-trip difference is smaller than 10 µGal, this type of gravimeter could show larger systematic bias values of 10–20 µGal between individual instruments (Tanaka et al. 2010). For a robust estimation, we employed this uncertainty rather than the round-trip measurements.

2.2 GNSS data

Continuous GNSS observations have been made in the vicinity of the above mentioned gravity measurement sites, and three-dimensional daily coordinates are available (Nishimura et al. 2023). Figure 3 shows the coseismic displacement due to the 2023 M6.5 event; this value was obtained by taking the difference between the April 27–May 4 and May 6–8 daily coordinates. The coseismic displacement was used for constructing the fault models in "Results" and "Discussion" sections.

2.3 A "dynamic" gravity anomaly

The concept of a gravity anomaly is usually used to study spatial variations in the density structure of the subsurface. Here, we consider a gravity anomaly to be related to the temporal gravity change, as was done in Tanaka et al. (2018). The gravity difference between two periods includes a component originating from the vertical movement of the crust that occurred between them. The contribution is proportional to the vertical movement and is divided into two effects: the apparent effect of the change in instrumental height (free-air effect) and the effect of the attraction due to the crust replacing the atmosphere (Bouguer effect). The residual gravity change obtained by removing these two effects represents the contribution of subsurface mass redistribution, apart from nontectonic effects.

In this study, a free air gradient of − 3.086 µGal/cm and a Bouguer plate with an average crustal density of 2.4 g/cm^3, which was obtained from a gravity survey in the area (Sawada et al. 2012), were employed to calculate the dynamic gravity anomalies. For the vertical movement

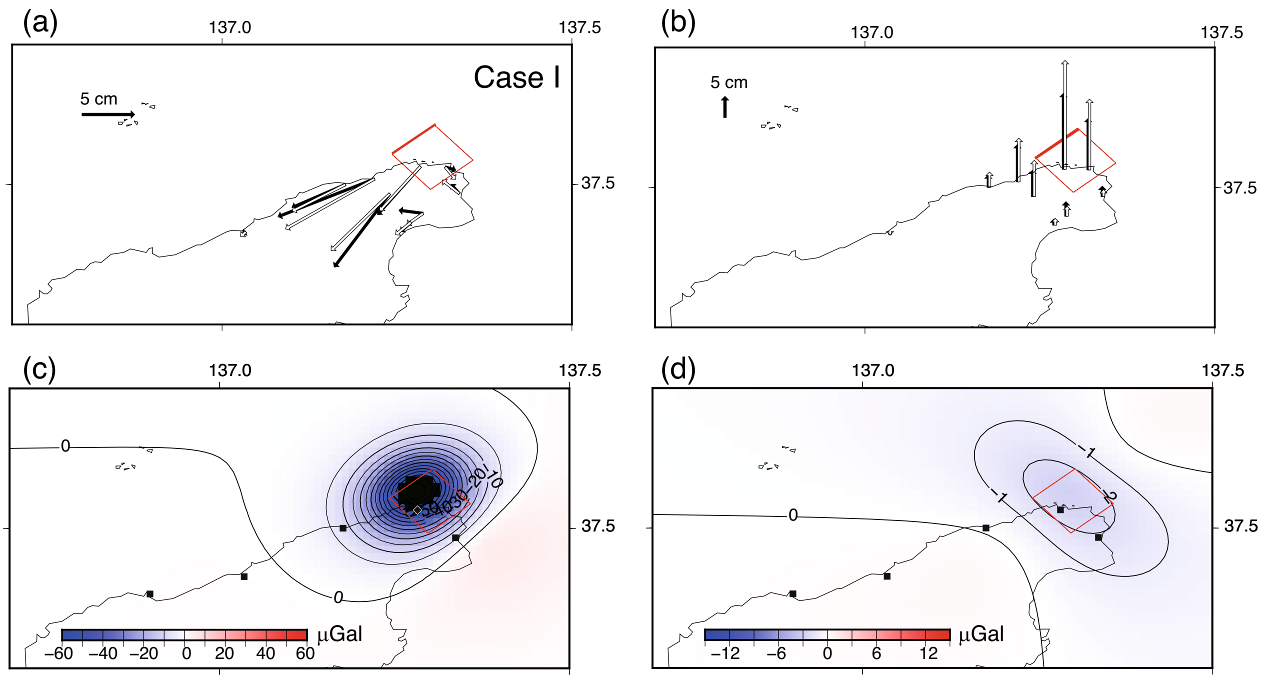

Fig. 3 Coseismic fault slip model. The horizontal and vertical displacements observed at the GNSS stations are shown by the black arrows in **a** and **b**, respectively. The fault model is shown by the red line with the thick line representing the top edge. The calculated displacements are superimposed by white arrows. **c** Gravity change theoretically calculated for the same fault model. **d** Contribution of subsurface dilatation to the total gravity change shown in **c**. The units of **c** and **d** are μGal

between two periods, the coseismic vertical displacements described in the previous section that were used to evaluate the displacement from March 7 to May 4 and that from May 9 to May 18 were negligible, considering the uncertainty of gravity observations (Additional file 1).

2.4 Groundwater contribution

2.4.1 Groundwater model

Nontectonic mass redistribution by surface fluids (e.g., the atmosphere, ocean, terrestrial water, and snow) also changes gravity. Groundwater fluctuations are a major factor and are known to produce signals at the scale of μGal or greater (Kazama et al. 2012; Crossley et al. 2013). Accurately estimating all the behaviors of groundwater in the vicinity of an observation site is extremely difficult because accurate subsurface local permeability structures are rarely understood and sites for groundwater level monitoring are limited. However, the behavior of unsaturated groundwater originating from rainfall can be estimated with relatively high accuracy. In this section, the method for estimating the gravity difference due to unsaturated groundwater flow between March and May 2023, when pre- and postearthquake gravity observations were made, is described. Gravity changes due to other nontectonic effects will be discussed in "Discussion" section.

We used GWATER-1D software, which calculates the vertical flow of unsaturated groundwater in a homogeneous semi-infinite medium and the associated gravity change (Kazama et al. 2012). The input is the effective precipitation calculated from precipitation and evapotranspiration. The fluid flow is governed by a nonlinear advection–diffusion equation such that the hydraulic conductivity and diffusion coefficient depend on the soil moisture content. The change in gravity is finally computed from the soil moisture profile via Newton's law. Owing to the large uncertainty in the soil parameters, the range of gravity changes was constrained for different model parameters rather than determining only the optimal model, as in Tanaka et al. (2018).

2.4.2 Input data

The effective precipitation was calculated on the basis of the daily precipitation, temperature, humidity, wind speed and daylight hours from Jan. 2021 to Sep. 2023, which were obtained at the Japan Meteorological Agency (JMA) AMeDAS station in Suzu city (http://www.data.jma.go.jp/obd/stats/etrn/index.php; the location is shown in Fig. 1).

2.4.3 Settings for the soil parameter range

In the vicinity of the SZHK absolute gravity measurement site, mainly fine-grained soils with clay aggregates and gleysols are distributed (G1k1t1 and F2a2t1 of the Japanese soil system classification, https://soil-inventory.rad.naro.go.jp/figure.html). Considering the low hydraulic conductivity of these soils (Carter and Bentley 1991), we set the hydraulic conductivity range used in the following calculation to 10^{-7} to 10^{-9} m/s. For the diffusion coefficient, we could not find data corresponding to these soils. Therefore, we set the range of the diffusion coefficient as wide as possible, on the basis of the diffusion coefficients of common soils (e.g., Ishida et al. 1990): 10^{-4} to 10^{-9} m^2/s.

The maximum and minimum soil moisture contents were fixed to the default values of the software ($\theta_{min} = 0.28$ and $\theta_{max} = 0.52$). However, we changed the convergence of the moisture content, θ_0, to that at a sufficient depth below the groundwater table. Four different values were taken for comparison, by dividing the interval between the maximum and minimum soil moisture contents into approximately 5 equal parts [0.32, 0.38 (software default), 0.42 and 0.46].

As a result, calculations were performed for 72 pairs of soil parameters.

2.4.4 Comparison data

To further constrain the range of soil parameters, the gravity change estimated by GWATER-1D was compared with the observed gravity change in specific periods. At SZHK, a similar absolute gravity measurement was conducted in September 2023. The gravity change with respect to the May 2023 measurement was approximately +3 μGal. No significant crustal deformation was observed during this period, suggesting that the gravity difference reflects mainly the influence of groundwater (Additional file 1).

In addition, the computed soil moisture content was compared with other results of simulations for the soils in Wajima city, published by the National Agriculture and Food Research Organization (https://soil-inventory.rad.naro.go.jp/). The simulation was based on observed weather and soil data. The average seasonal change over 30 years was compared with our groundwater model.

2.5 Coseismic fault model

From a geodetic inversion of the coseismic displacement ("GNSS data" section), we determined a rectangular fault model with a uniform shear slip, assuming the elastic half-space model of Okada (1985). The strike and dip angles were fixed at those of the JMA centroid moment tensor (CMT) solution. For convenience, we refer to

Table 1 Candidate fault parameters (* = fixed)

Flt	Long	Lat	D	L	W	Θ	δ	α	ΔU^s	ΔU^t	$\overline{\chi}_{1or2}$ / $\overline{\chi}_{GNSS}$	δg / Δg
Units	Degree		km			Degree			M		–	μGal
Case I: shear slip only												
A	137.243	37.543	6.0	7.1	8.9	49	34	96	1.94	0.0	6.84^{1} / 2.83	−2.5 / −56.5
Case II: $\overline{\chi}_1$ is the smallest, $\lvert\delta g/\Delta g\rvert > 0.15$												
A	fixed as for Case I							86	1.44	0.0	3.24^{1}	−7.5
B	137.233	37.528	0.5	5.0	2.5	90*	90*	–	0.0	0.2	3.22	−44.7
Case III: $\overline{\chi}_1$ is the second smallest, $\lvert\delta g/\Delta g\rvert > 0.15$												
A	fixed as for Case I							86	1.44	0.0	3.32^{1}	−6.6
B	137.233	37.528	0.5	5.0	2.5	90*	90*	–	0.0	0.25	3.31	−43.8
Case IV: $\overline{\chi}_1$ is the smallest, $\delta g < -5$ μGal												
A	fixed as for Case I							96	1.44	0.0	2.99^{1}	−5.6
B	137.233	37.528	0.5	5.0	2.5	90*	90*	–	0.0	0.2	2.89	−45.4
Case V: $\overline{\chi}_2$ is the smallest, $\lvert\delta g/\Delta g\rvert > 0.15$												
A	fixed as for Case I							86	1.64	0.0	2.78^{2}	−7.8
B	137.233	37.528	0.5	5.0	2.5	90*	90*	–	0.0	0.3	2.77	−50.2
Case VI: $\overline{\chi}_2$ is small, $\lvert\delta g/\Delta g\rvert > 0.15$, Δg is closer to Δg_{obs}												
A	fixed as for Case I							86	1.54	0.0	2.92^{2}	−7.7
B	137.233	37.528	0.5	5.0	2.5	90*	90*	–	0.0	0.3	2.95	−47.4

D: depth of the top edge of the fault *L*: length *W*: width Θ, δ, α: strike, dip and rake angles. The superscript values 1 or 2 represent $\overline{\chi}_1$ or $\overline{\chi}_2$, respectively this fault as Fault A. The obtained fault model parameters are listed in Table 1 (Case I). The gravity change due to fault slip was calculated via the analytic formula of Okubo (1992) on the basis of the same half-space model. In "Results" section, the results show that this gravity change is insufficient to explain the observed gravity anomaly.

2.6 Additional tensile fault representing fluid flow

In "Discussion" section, we examine whether subsurface fluid flow could explain the gravity data, assuming that fluid paths are approximated by a tensile fault in the elastic half space. By adding a tensile fault, the fault parameters of Fault A listed in Case I of Table 1 need to be adjusted. The fault parameters for the tensile fault and Fault A are determined with a grid search algorithm so that the sum of the displacements and gravity changes due to these faults, as calculated with Okada (1985) and Okubo (1992), better explains both the GNSS and gravity data. The density of the fluid was set to 1000 kg/m^3.

To reduce the number of parameters in the grid search, for Fault A, we fixed all the parameters except for the slip amount ($\equiv \Delta U^s$) and rake angle. For the tensile fault, we inferred the location, depth, length, width and opening amount ($\equiv \Delta U^t$) as free parameters. The strike and dip angles were fixed at 90° (i.e., dikes in the east–west direction), on the basis of the geological structure and a trial calculation ("The case when the coseismic fault opens" to "Overview of the tensile fault model" sections).

The grid search was performed to minimize the chi-square value described below. First, we define

$$\chi^2_{\mathrm{GNSS}} \equiv \sum_{i=1}^{N} \left(\frac{\left(u^i - u^i_{\mathrm{obs}}\right)^2}{\sigma_H^2} + \frac{\left(v^i - v^i_{\mathrm{obs}}\right)^2}{\sigma_H^2} + \frac{\left(w^i - w^i_{\mathrm{obs}}\right)^2}{\sigma_V^2} \right)$$

where (u^i, v^i, w^i) denote the east, north and height components of the calculated displacement at the i-th observation site, respectively, and those with obs denote the observed displacement. $N(=9)$ denotes the number of observation sites. Considering that the ratio of the uncertainties of the horizontal and vertical components was approximately 1:3 (Ohta and Ohzono 2022), we set σ_H and σ_V as 3 mm and 9 mm, respectively. Next, we define

$$\chi_g^2 \equiv \frac{\left(\Delta g - \Delta g_{\mathrm{obs}}\right)^2}{\sigma_g^2}$$

where $\sigma_g = 2$ μGal and Δg and Δg_{obs} represent the computed and observed gravity changes at SZHK. Here, the nontectonic effects of -3 μGal, which is an average of −4 to −2 μGal ("Other nontectonic contributions" section and Table 4), were removed from the observed total gravity change (i.e., $\Delta g_{\mathrm{obs}} = -44$ μGal). The gravity data obtained at stations other than SZHK were not sufficiently accurate to constrain the fault parameters (Table 2).

Table 2 Observed gravity change Δg, gravity anomaly δg, and vertical displacement w_{obs}

Site	Δg	δg	w_{obs}	σ
Units	μGal	μGal	cm	μGal
SZHK	−47	−10	18	2
SZMS	−16	−12	2	10–20
SZOT	−7	−1	3	
0971	−13	*	*	
NTWT	−8	*	*	

* The vertical displacement was insignificant

Because the number of gravity data points (=1) was much smaller than the number of GNSS data points, we minimized the following quantity

$$\overline{\chi}_1 \equiv \sqrt{\left(\overline{\chi}^2_{\mathrm{GNSS}} + \chi_g^2\right)}, \overline{\chi}_{\mathrm{GNSS}} \equiv \sqrt{\chi^2_{\mathrm{GNSS}}/3N}$$

so that GNSS data and gravity data have equal weights. For comparison, we also used

$$\overline{\chi}_2 \equiv \sqrt{\left(\chi^2_{\mathrm{GNSS}} + \chi_g^2\right)/(3N+1)}$$

where the difference in the number of data points between the GNSS and gravity measurements was not considered. Furthermore, we note that models that reproduce Δg_{obs} do not necessarily produce large gravity anomalies as observed ("Observed gravity change" section). Therefore, we imposed an additional condition in which the ratio of the calculated gravity anomaly to the total gravity change was greater than 15% to extract models that could reproduce the observed ratio ($\delta g_{\mathrm{obs}}/\Delta g_{\mathrm{obs}} \cong -7/-44 = 16\%$).

3 Results

3.1 Observed gravity change

Table 2 shows the observed gravity changes, coseismic vertical displacements and gravity anomalies obtained by the method described in "Gravity data", "GNSS data" and "A "dynamic" gravity anomaly" sections. Significant uplifts were observed near the epicenter of the 2023 M6.5 earthquake and negative gravity changes were detected at all the observation sites. At SZHK, where the uplift was the largest, the amplitude of the gravity change was the largest, exceeding 40 μGal. This change was well above the error of observations. The gravity anomaly was −10 μGal, which was also significant. At the other sites, the gravity changes were approximately −10 μGal, which was small compared with the error of observations. However, those changes tended to decrease with increasing distance from the epicenter. At SZMS, the gravity anomaly was comparable with that at SZHK, but the reliability of the result was lower, considering the error of observations. In the following, we focus on the gravity anomaly at SZHK.

Table 3 Candidate soil parameter sets for the groundwater model

Model	k_s	d_s	θ_0	Δg_1	Δg_2
Units	**m/s**	**m^2/s**	**m^3/m^3**	**μGal**	**μGal**
1a	5e−8	1e−5	0.38	+0.7	−0.9
1b	1e−7	1e−7	0.38	−0.6	−2.5
2	5e−8	1e−5	0.32	+0.3	−2.5
3	5e−8	1e−5	0.42	+0.4	−0.5
(obs.)	–	–	–	+2.5	−11

Δg_1: observed gravity change from May 2023 to September 2023, Δg_2: March 2023 to May 2023

3.2 Groundwater contribution

First, we considered the case of $\theta_0 = 0.38$. From the calculated results, we excluded unreasonable sets of hydraulic conductivity k_s and diffusion coefficient d_s values in the following manner. The results that revealed a large increasing/decreasing trend over the entire period, meaning that the soil moisture content did not converge, were eliminated. Next, parameter sets that could not explain the gravity change of +3 μGal observed from May to September within 6 μGal were excluded. Consequently, only two sets, shown by Models 1a and 1b in Table 3, remained.

Figure 4 shows the results for these two sets. The lower envelope of the orange curve in (a) shows that the effective precipitation reached a maximum in winter, which corresponded to the largest peak in gravity (blue curve). Furthermore, in summer, precipitation was infrequent, but large daily rainfall events occurred, which corresponded to the second largest peak in gravity. The change in gravity during the whole period was approximately 3 μGal. In the figure, the three red diamonds indicate when the gravity observations were made. The gravity differences between May and September (Δg_1) and

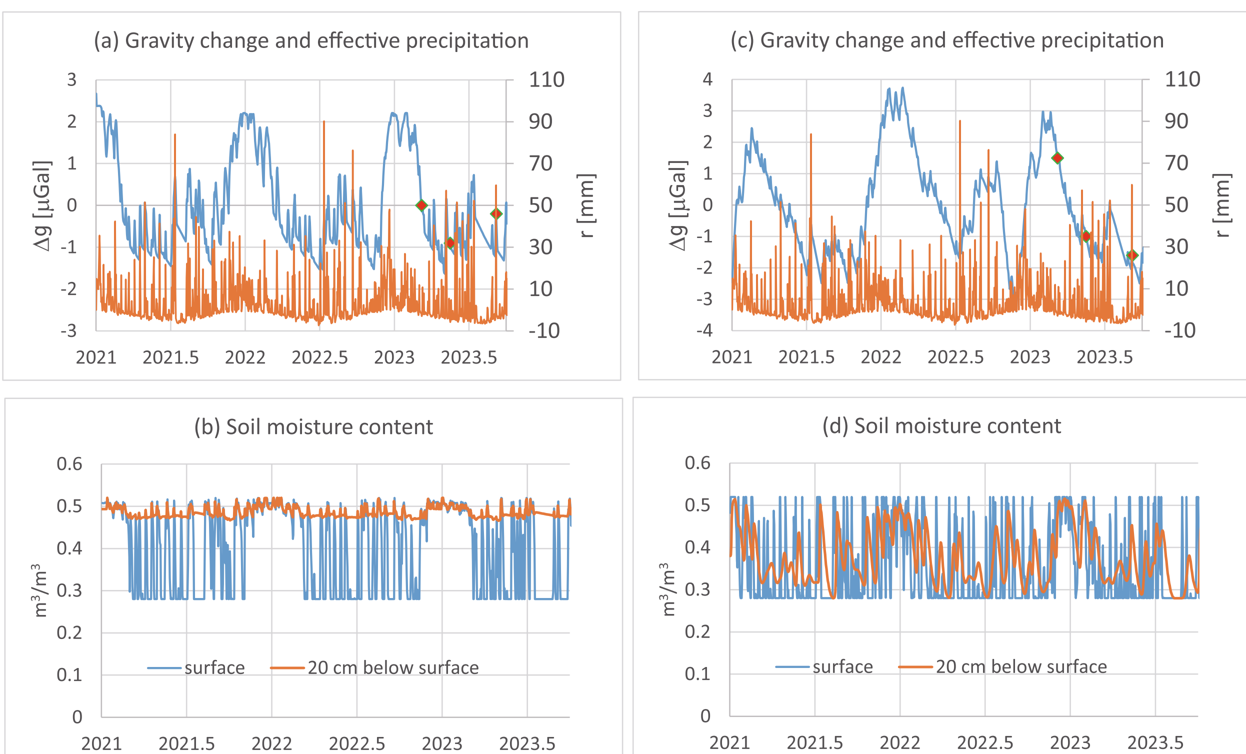

Fig. 4 Groundwater model. **a** Daily gravity change (blue) and effective precipitation (orange). Case for $k_s = 5 \times 10^{-8}$ m/s and $d_s = 10^{-5}$ m^2/s. The red diamonds indicate when the gravity observations were made. **b** Soil moisture content at two different depths corresponding to **a**. **c** Same as **a** but for $k_s = 10^{-7}$ m/s and $d_s = 10^{-7}$ m^2/s. **d** Soil moisture content at two different depths corresponding to **c**

Table 4 Observed and calculated gravity changes at SZHK from March to May 2023

kinds	Δg (μGal)	Remarks
a. Observation		
Total change	− 47 ± 2	Including correction errors
BG anomaly	− 10 ± 2	Corrected with GNSS-observed height of 18 cm
b. Sea level changes		
Coseismic decrease	− 0.9 (UL)	Mass attraction (upper limit)
Seasonal change	− 0.2 (UL)	Ocean bottom pressure by satellite gravimetry
c. Groundwater (GW)		
Unsaturated GW	− 2.5 to − 0.5	GWATER-1D, AMeDAS, Δg_2 in Table 3
Unconfined GW	(− 2.7)	Rapid horizontal flow after earthquake (unlikely)
Confined GW	–	Poroelastic flow, counted in the dilatation below
Sum (b + c)	− 4 to − 2	
d. Tectonic effects		
Dilatation	− 2	Fault A (shear slip)
Dilatation + fluid mass	− 6 to − 4	Fault B (vertical tensile)
Sum (d)	− 8 to − 6	Cases II–VI in Table 1
Total (b + c + d)	− 12 to − 8	

between March and May (Δg_2) were smaller than 1 μGal, which was less than the measurement uncertainty.

Figure 4c shows the result for Model 1b in the same manner. The gravity change showed a pattern similar to a triangle wave, implying that the attenuation of soil moisture was relatively slow. The change in gravity during the whole period was approximately 6 μGal. The gravity difference between May and September was − 0.6 μGal and that from March to May was − 2.5 μGal, which could partly explain the negative gravity anomaly of − 10 μGal.

Figure 4b/d shows the soil moisture content at two different depths for Model 1a/b. Abrupt changes from $\theta_{\min}$ to $\theta_{\max}$ occurred at the surface in response to each rainfall event and that these responses were weaker at a depth of 20 cm and that long-term behaviors were more easily discernible. The tendency for the highest values to occur in winter and the second highest values to occur in summer exhibit good agreement with the results of another simulation, although there is a systematic bias caused by setting $\theta_{\min}$ to approximately 0.3 in our model, indicating that the parameter sets of Model 1a/b are reasonable (Additional file 1). A more careful examination reveals that (b) is closer to the simulation than (d) in that it reproduces the fact that the variability decreases more rapidly with depth.

For $\theta_0 = 0.32$, screening the parameter sets by the same criteria caused only the same set as Model 1a above to remain (Model 2 in Table 3). The gravity differences Δg_1 and Δg_2 were 0.3 μGal and − 2.5 μGal, respectively. The result of this model was difficult to distinguish visually from that of $\theta_0 = 0.38$. For $\theta_0 = 0.42$, a similar result was obtained and the gravity difference from March to May was − 0.5 μGal. For $\theta_0 = 0.48$, unnatural trends occurred, and no rational solution was obtained.

On the basis of the above results, the March–May gravity differences from this groundwater model ranged from − 2.5 to − 0.5 μGal and could explain a maximum of − 2.5 microGal of the observed gravity anomaly of − 10 μGal (Table 4).

3.3 Contribution of the coseismic fault model

The coseismic displacement calculated for the fault parameters of Case I in Table 1 is superimposed on the data in Fig. 3a, b. The good agreement with the observations indicates that a single fault with uniform slip can reproduce the observed deformation pattern, especially the horizontal component, well. Figure 3c shows the gravity change calculated using the same fault parameters. By removing the free-air and Bouguer effects from (c) and using the calculated height, we theoretically obtained the contribution of subsurface dilatation (Fig. 3d). A comparison of (c) and (d) reveals that the latter was only approximately 5%. At SZHK, the total change was − 56.5 μGal and the dilatation effect was − 2.5 μGal, corresponding to 4.4%. The ratio of the observed gravity anomaly to the observed total gravity change was greater than 20% ("Observed gravity change" section). Even if the fault parameters were adjusted so that the calculated height change at SZHK completely agreed with the observed height change, the dilatation effect would explain only approximately 5% of the variation (~ − 2 μGal) as long as only shear slip was assumed. In addition, considering the characteristics of Green's function for shear slip, heterogeneities in the Earth structure and slip distributions cannot reproduce the relative ratio of the gravity anomaly to the total gravity change (Additional file 1).

4 Discussion

4.1 Other nontectonic contributions

4.1.1 Sea level changes

The May 2023 earthquake caused a seafloor uplift in the northern part of the epicentral area. The uplift of the seafloor moved seawater away, creating a secondary negative change in the gravity field. This contribution can be estimated theoretically by solving the sea-level equation, which has often been used in the field of glacial isostatic adjustment (Farrell and Clark 1976). Here, owing to the expected small signal, loading deformation was ignored, and only the gravitational pull of seawater was considered for a simplified estimate. The calculation of the coseismic vertical displacement presented in "Contribution of coseismic fault model" section reveals that the maximum uplift of the seafloor was approximately 30 cm. The distance from SZHK to the coast was 130 m and the elevation was 30 m. Considering this geometry and using Newton's law, we estimated the upper limit of the gravity change, assuming a 30 cm uplift of the entire seafloor. The result was − 0.9 μGal, which was only 9% of the observed gravity anomaly of − 10 μGal.

In addition to seafloor uplift, oceanographic seawater mass movements caused gravity changes. The most prominent variation in the Sea of Japan was seasonal. Satellite gravity observations indicate that ocean bottom pressure reached a maximum in winter, with peak-to-peak amplitudes of 10 to 20 cm (CNES GRACE plotter, https://thegraceplotter.com/). We estimated the gravity change from March to May due to this seasonal variation, considering the geometry used in the previous paragraph. The result was only − 0.2 μGal.

4.1.2 Unmodeled groundwater contributions

We examined whether contributions not included in the unsaturated groundwater model ("Groundwater contribution" section) could be the main cause of the gravity anomaly.

Confined groundwater is known to flow with frame deformation around pores. Hence, coseismic deformation may cause poroelastic fluid flow. The contribution to the gravity change would theoretically be almost the same as the contribution of the change in the elastic volumetric strain, which was estimated in "Contribution of coseismic fault model" section, although there are differences in the temporal evolution between elastic and poroelastic materials. Therefore, this effect is not considered to be a primary cause.

Owing to the lack of available data on groundwater levels around SZHK, it is very difficult to estimate the contribution from variations in unconfined groundwater accurately. In the following text, the possible contributions of unconfined groundwater are discussed.

First, the coseismic decrease in sea level relative to that at the observation site ("Sea level changes" section) may have caused a horizontal difference in groundwater pressure, which could have resulted in the discharge of terrestrial groundwater into the sea. The uplift at SZHK is 18 cm. Assuming a Bouguer plate with a porosity of 0.38, the decrease in gravity is estimated to be 2.7 μGal, which could partly explain the gravity anomaly. Here, a porosity value of 0.38 was chosen to maintain consistency with the value of θ_0 adopted in groundwater Models 1a and 1b ("Groundwater contribution" section and Table 3). However, given the inferred low hydraulic conductivity and diffusion coefficient of the soils ("Groundwater contribution" section), it is unlikely that groundwater would have flowed out rapidly within two weeks from immediately after the earthquake to the time of gravity measurement (one could confirm this by a simple dimensional analysis for a distance of 130 m, k_s of ~10^{-7} or d_s of ~10^{-5}). Furthermore, as far as the authors were able to ascertain, there were no reports of a significant decrease in groundwater levels immediately after the earthquake near SZHK.

Next, we considered a slower variation in the unconfined groundwater table from March to May. Assuming a porosity of 0.38, a 40 cm decrease in the groundwater level would result in a gravity change of − 6 μGal. However, the average monthly tide level at Wajima is ~ 20 cm higher in summer (Geospatial Information Authority of Japan (GSI), https://www.gsi.go.jp/kanshi/tide_furnish.html). The phase is opposite to that of changes in ocean bottom pressure from satellite gravity observations ("Sea level changes" section) because of the steric component. The tide level change from March to May 2023 was + 11 cm according to the same GSI data. In general, near the ocean, groundwater levels are linked to sea level. Therefore, it is unlikely that groundwater levels decreased from March to May, at least intuitively. Further investigation is needed to determine whether a decrease in the groundwater table exceeding 40 cm occurred between March and May.

4.1.3 Summary of the nontectonic contributions

Table 4 summarizes the nontectonic gravity changes described above. Unsaturated groundwater, mainly from rainfall, reached − 2.5 μGal. Relative decreases in sea level due to coseismic deformation and seasonal variation caused negative changes reaching − 0.9 μGal and − 0.2 μGal, respectively. The contribution from the poroelastic fluid flow of confined groundwater can be considered the elastic dilatation effect, neglecting temporal evolution. Unconfined groundwater could cause negative gravity changes of up to − 2.7 μGal if rapid flow occurred immediately after the earthquake, but this is unlikely. Excluding the last contribution, the nontectonic effects could explain − 2 to − 4 μGal of the observed − 10 μGal anomaly. Moreover, the elastic dilatation effect calculated by a well-established dislocation theory could explain − 2 μGal ("Contribution of coseismic fault model" section). To explain the remaining gravity anomalies of − 6 to − 4 μGal with changes in the groundwater table, one would have to show that the groundwater table decreased by approximately 40 cm (corresponding to − 6 μGal) from March to May.

4.2 Tectonic contributions assuming crustal fluid flow

4.2.1 The case in which the coseismic fault opens

On the basis of the results of the previous section, we examine whether the remaining − 4 to − 6 μGal anomalies could be explained by adding a hypothetical tensile fault. First, we investigated the case in which the coseismic fault (Fault A) opened. We found from trial-forward calculations that such a model, when given fluid volumes to explain the − 4 to − 6 μGal anomalies, produced a radial horizontal displacement pattern around SZHK, causing a large discrepancy with the displacements observed at 9094, SZMS, SZID and 0523 (Figs. 1 and 3a). Therefore, we excluded the possibility of opening the coseismic fault as a fluid pathway. Similarly, the case in which a shallow extension of the fault opens could not explain the observed displacements well.

4.2.2 Overview of the tensile fault model

Next, we considered a tensile fault with a different inclination than that of Fault A. One possibility is to assume a vertical flow of fluid, which would be natural, considering buoyancy. Such a flow can be represented by the horizontal opening of a vertical tensile fault. Vertical tensile faults (or dikes) generally tend to be parallel to the direction of compression under the regional stress field (i.e., NW–SE). However, an east-west-oriented seismic anisotropy resulting from geologic features is indicated in this area (Okada et al. 2024), indicating that cracks tend to develop in the east-west direction.

Figure. 3a shows that the computed horizontal displacements at SZMT and SZOT are shifted eastward relative to the observed displacement whereas that at 9095 is shifted westward. Moreover, Fig. 3b shows that the computed uplifts at SZHK and 9094 are overly large. Tilting the direction of the fault slip to the west should eliminate the disagreement with the observations at SZMT and SZOT and leave a southward displacement at 9095. Adding a dike along the east-west direction near SZHK would produce a southward displacement at 9095 and subsidence around SZHK. Therefore, a model that includes a dike in the east-west direction is expected to have better agreement with the observations than Case I.

In addition, the coseismic crustal deformation caused extensional stress in the N-S direction, which tends to open cracks along the E-W direction (Additional File 1).

On the basis of the above considerations of geological, geometric and dynamic aspects, the azimuth of the vertical tensile fault was assumed to be 90°. We refer to this tensile fault as Fault B (Fig. 5a). The actual fluid pathway may consist of numerous smaller cracks in the east-west

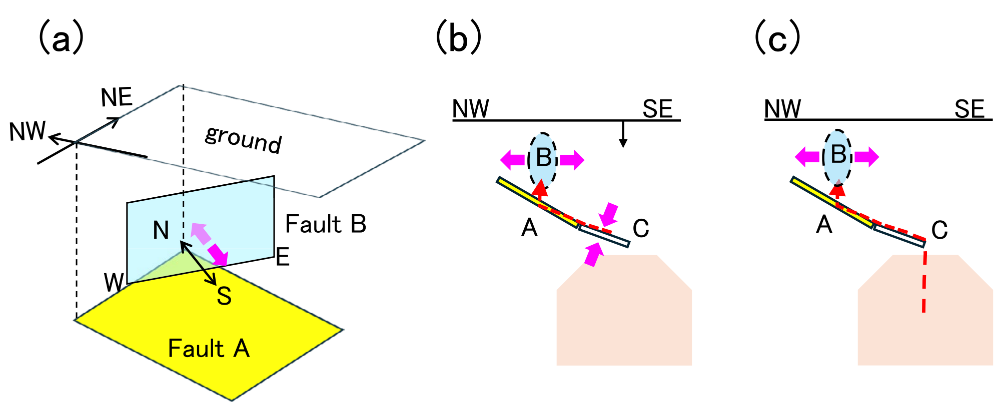

Fig. 5 Model schematic. **a** Fault planes. A: Coseismic fault, B; vertical tensile fault imitating fluid flow. **b** The case in which fluids are supplied from Fault C, where the accumulation of fluids was suggested before the earthquake (Nishimura et al. 2023), to Fault B. **c** The case in which fluids are supplied from the deeper fluid-abundant region to B through A and C

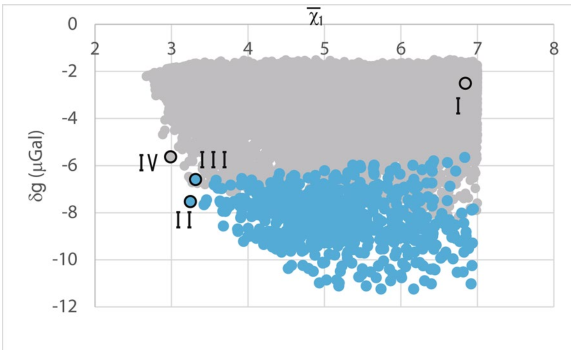

Fig. 6 $\overline{\chi}_1$ and the gravity anomaly for each fault parameter set in the grid search. Smaller values of $\overline{\chi}_1$ indicate better agreement between the model and observations. The circles marked by I–IV correspond to Cases I–IV in Table 1. The blue dots represent the parameter sets that reproduce the observed gravity change

direction. Because of the sparse gravity observations, our model cannot represent such local structures.

As a source of fluids flowing into Fault B, the slow slip region located below the epicenter of the May 2023 earthquake was considered (the source parameters are those for Period C in Nishimura et al. 2023). We refer to this fault as Fault C. The amount of "closing" of Fault C could be given so that the volume of fluids flowing into Fault B matched the volume flowing out of Fault C (Fig. 5b). However, such a model caused subsidence of the southern part of Suzu city, which could not explain the uplift at SZMS, SZID and 0523 (Fig. 1).

An alternative source of fluid could be from a region deeper than Fault C, where fluid is abundant (Nakajima 2022; Nishimura et al. 2023). We assume that this region is connected to Faults A, B and C and that the crustal deformation associated with outflow from this deeper fluid-rich region is too small to detect. The amount of

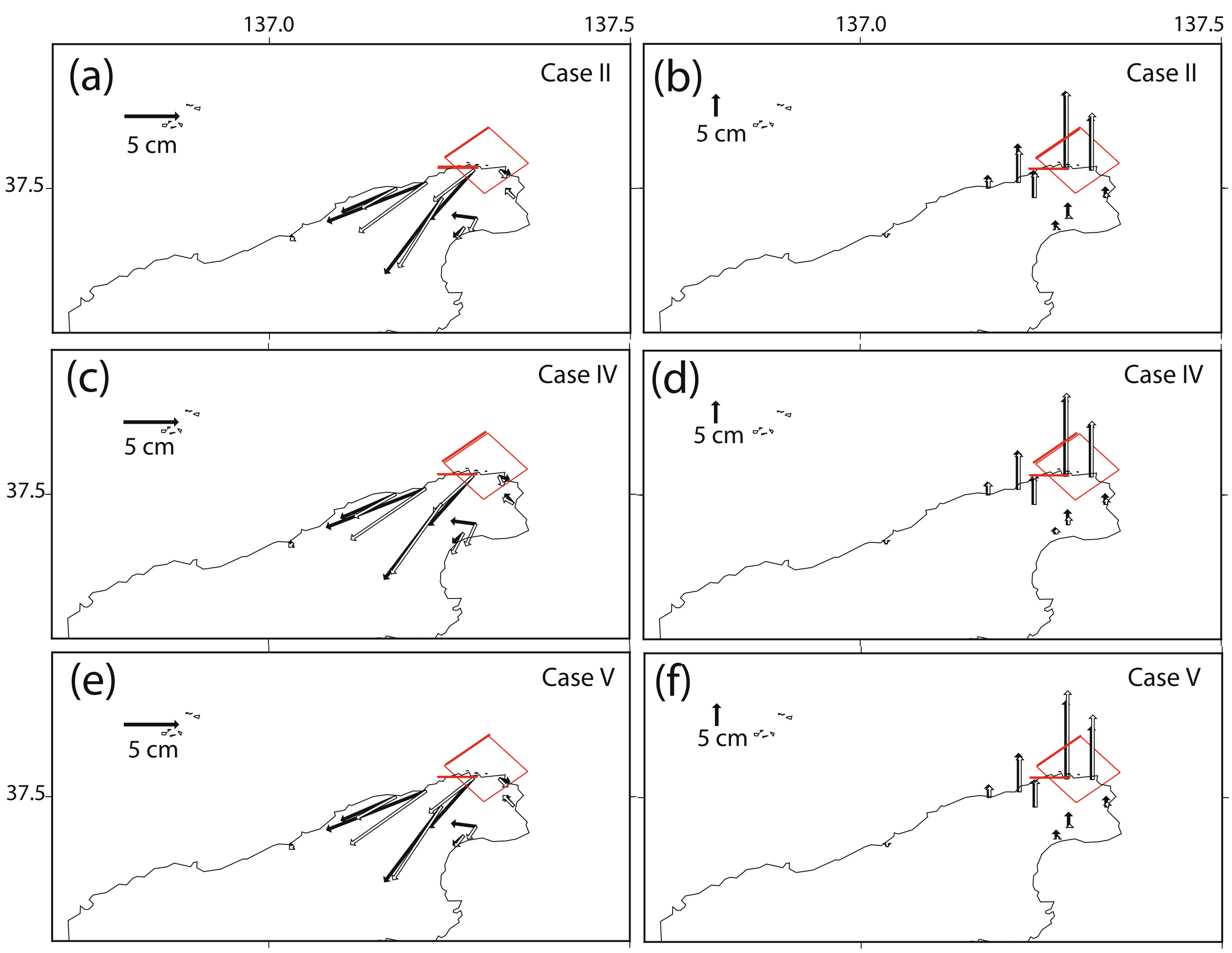

Fig. 7 Displacement fields calculated for the selected parameter sets (white arrows). The observed displacements are shown by the black arrows. (**a**/**b**), (**c**/**d**) and (**e**/**f**): horizontal/vertical displacements for Cases II, IV and V in Table 1, respectively. The strike of the tensile fault is represented by the thin red line in the east–west direction

fluid flowing into and out of Fault C is equal, and the effective opening of Fault C is zero (Fig. 5c). We adopt this assumption below.

4.2.3 Grid-search results

We present the results of estimating the parameters of Faults A and B on the basis of the method described in "Additional tensile fault representing fluid flow" section.

Figure 6 shows $\overline{\chi}_1$ for different fault model parameters in the grid search. In the figure, the upper right circle marked by I represents the case in which only the shear slip is considered (Case I in Table 1). The vertical axis denotes the computed gravity anomaly. The total gravity change was −56.5 μGal due to the overestimated uplift at SZHK (Fig. 3b), which resulted in a large $\overline{\chi}_1$ value (=6.84). The computed gravity anomaly was −2.5 μGal, which did not reproduce the observations as already mentioned ("Contribution of coseismic fault model" section). Many parameter sets occurred for which the value of $\overline{\chi}_1$ was less than 6.84. However, the parameters that

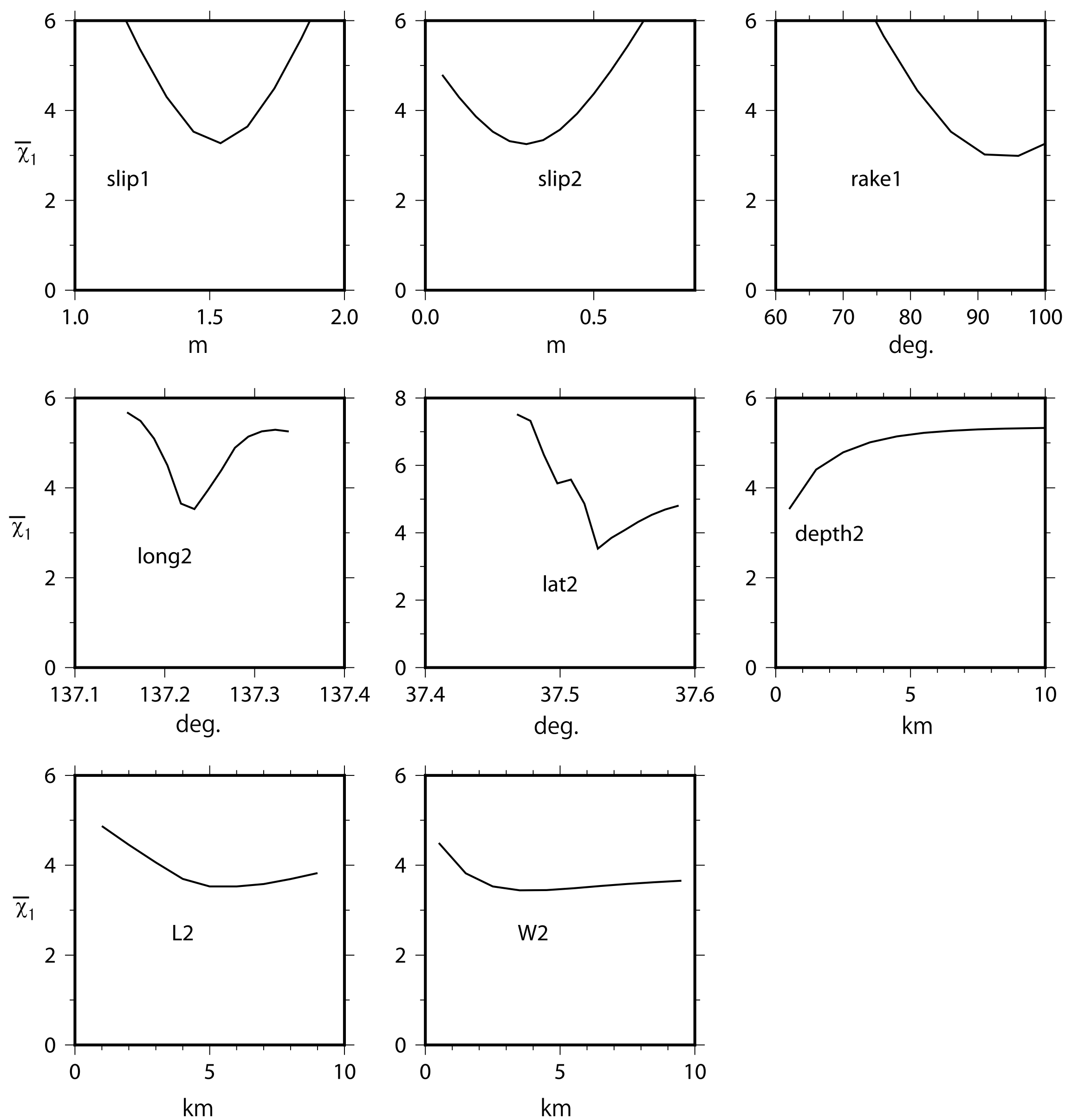

Fig. 8 Dependence of $\overline{\chi}_1$ when each fault parameter for Case II is moved. "slip1" and "slip2" denote the amount of shear slip of Fault A and the fault opening of Fault B, respectively. "rake1" is the rake angle of Fault A. "long2", "lat2", "depth2", "L2" and "W2" are the longitude, latitude, depth, length and width of Fault B, respectively

minimize $\overline{\chi}_1$ produced a gravity anomaly of only approximately −2 μGal (the leftmost gray dot). Therefore, we extracted the parameter sets for which the ratio of the calculated gravity anomaly to the total gravity change was greater than 15% (the blue dots).

Among these blue dots, the case with the smallest $\overline{\chi}_1$ was marked with II in Fig. 6. The parameters are shown in Case II of Table 1. As expected, the rake angle of Fault A shifted slightly to the west. The tensile fault was located west of SZHK along the coastline (Fig. 7a) and its depth was shallow (Table 1). The computed total gravity change and gravity anomaly due to both faults were −44.7 μGal and −7.5 μGal, respectively, which successfully reproduced the remainder of the observations minus nontectonic effects (−44 μGal, "Additional tensile fault representing fluid flow" section). Figure 7a, b shows the computed displacement field. Compared with Case I, the agreement for the vertical component at SZHK was significantly improved because of the increased weight in gravity. The computed uplift at SZHK was 17.5 cm, which was very close to the observed 18 cm. $\overline{\chi}_{GNSS}$ for Case II was 3.22, which was greater than 2.83 for Case I, indicating that Case II explained the gravity data better than did Case I by slightly sacrificing the agreement with the GNSS data. Figure 8 shows the behavior of $\overline{\chi}_1$ when each parameter of Case II is moved. The results show that $\overline{\chi}_1$ has one minimum value for most parameters and that the minimum values were located near the Case II values shown in the table.

Figure 9a shows the total gravity change for Case II. Compared with Fig. 3c, the overall pattern of gravity change remained the same, but the magnitude of the change decreased because the overestimation of the change in height was eliminated as mentioned above. Figure 9b shows the spatial pattern of the gravity anomaly for Case II. Compared with Fig. 3d, a large negative anomaly was localized near SZHK. The volume of fluid was 2.5×10^6 m^3. The computed gravity anomalies from Faults A and B were −1.9 μGal and −5.6 μGal, respectively.

Case III in Table 1 shows the parameters such that $\overline{\chi}_1$ was the second smallest (Fig. 6). The difference from Case II was only the amount that the fault opened. The reproducibility of the GNSS and gravity data was nearly the same as that for Case II (Table 1).

Case IV in Table 1 shows the parameters that minimize $\overline{\chi}_1$ among the sets that produced gravity changes smaller than −5 μGal (Fig. 6). The location of the tensile fault was the same as that in Cases II and III, and only the rake angle was slightly different. As a result, the pattern of displacement in Case IV was almost identical to that in Case II, although agreement with the observed vertical displacement at SZHK in Case IV was slightly degraded (compare Fig. 7c, d with a, b). The computed total gravity change and gravity anomaly were also close to those of Cases II and III (Table 1). $\overline{\chi}_{GNSS}$ for Case IV improved to 2.89, which was nearly the same as that for Case I (2.83), indicating that Case IV accounted for the gravity data to some extent without sacrificing agreement with the GNSS data.

Next, Case V in Table 1 shows parameters that minimize $\overline{\chi}_2$ when the ratio of the gravity anomaly was greater than 15%. Only the amounts of shear slip and fault opening were slightly different from those in Cases II and III. As a result of the reduced weight on gravity, $\overline{\chi}_{GNSS}$ for Case V was better than that for Case I. Comparing Figs. 3a with 7e and 3b with 7f, the results show that the agreement in the vertical component was greatly improved. The computed gravity anomaly was sufficiently large. However, the amplitude of the computed total gravity change was larger than that of the observed change because of the overestimated uplift at SZHK (Fig. 6f). Case VI in Table 1 shows an example for which the computed total gravity change was closer

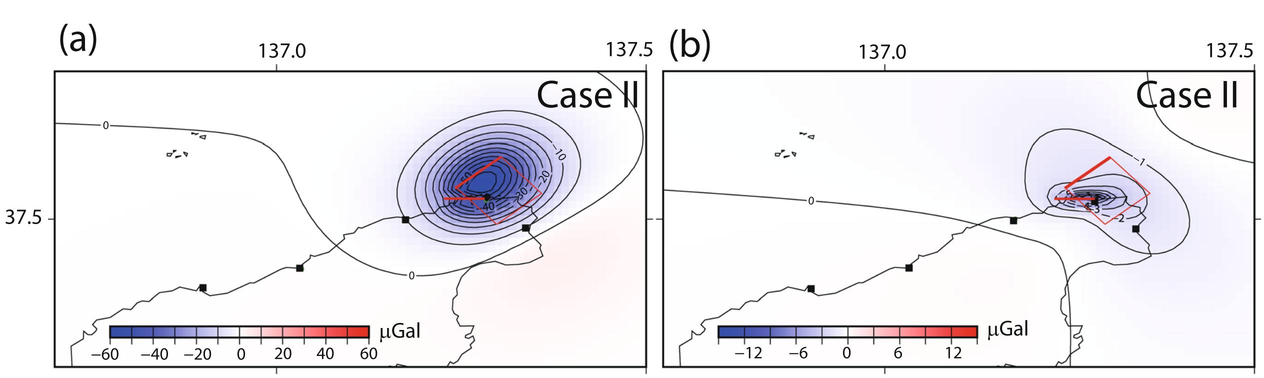

Fig. 9 Gravity change calculated for Case II. **a** Total gravity change. **b** Contribution of subsurface dilatation to the gravity change in **a**. The units are μGal

to the observation. $\overline{\chi}_{GNSS}$ for Case VI was smaller than those for Cases II and III. Only the amount of shear slip was different from that in Case V.

The above results indicate that placing an east–west vertical tensile fault west of SZHK and making its top edge shallower than the top edge of the coseismic fault could reproduce both GNSS and gravity data. This tendency did not strongly depend on the choice of function that is minimized in the grid search.

4.2.4 Geophysical implications

From the above results, the following results related to fluids can be derived. Before the May 2023 earthquake, ~ 3×10^7 m^3 of fluids had accumulated in the deeper-dipping fault (i.e., Fault C) (Nishimura et al. 2023). The May 2023 event broke the seal of preexisting cracks in the shallower part of the coseismic fault, which triggered an upward transient flow driven primarily by pressure differences and buoyancy. Such mechanisms can be found in the literature (e.g., Husen and Kissling 2001; Sibson 2020). Consequently, approximately 10% of the fluids (~ 3×10^6 m^3) moved into a region shallower than the coseismic fault (tensile Fault B). Nearly the same volume of fluids that flowed out of Fault C was likely fed immediately from the fluid-rich region below it (Fig. 5c). The estimated fluid volume on the order of 10^6 m^3 was within the range of fluid volumes (10^{6-8} m^3) which was indicated from an analysis based on injection-induced seismicity (Mukuhira et al. 2022).

Kato (2024) reported that the aftershock front migrated along the coseismic fault plane immediately after the May 2023 earthquake and noted that this shallowing could have been triggered by the upwelling of fluids (Fig. 3a, b of Kato (2024)). Our result was partly consistent with his result in that our model could explain the upward migration of fluids through the coseismic fault (Fig. 5c), although the vertical tensile fault could not explain a migration along an inclined plane. In addition, the location of the tensile fault coincided with the source region of the January 2024 M7.6 earthquake. This finding indicates that fluid upwelling might have been one of the factors that facilitated the January earthquake. Ma et al. (2024) suggested that the initial rupture process of the January event occurred within a fluid-rich fault zone.

Seismic tomography by Nakajima (2022) revealed that a region with high V_p/V_s values exists in the lower and upper portions of the source area of the 2007 Noto Peninsula earthquake. In addition, a region with high V_p/V_s values is located near the northeastern coastal area of Suzu city in both the lower and upper parts of the source of the May 2023 earthquake [V_p/V_s of F and G in Fig. 3 and the case for 5 km in Fig. S3 of Nakajima (2022) and Fig. 4 of Okada et al. (2024)]. The existence of such a region in the shallower portion than the earthquake source fault might indicate that the coseismic upwelling of fluids, inferred from our gravity observations, has been repeated in the past.

Even larger negative gravity anomalies, which could not be explained by elasticity dislocation theory, were observed in January 2024 at SZHK and NTWT after the M7.6 event (in preparation). As mentioned above, in these two areas, regions with high V_p/V_s values are located in the shallow and lower portions of the sources. These facts increase the possibility that the gravity anomaly between March and May reported in the present paper is related to tectonic activity rather than fluctuations in groundwater.

5 Conclusions

This paper reports the possibility that absolute gravity measurements captured coseismic crustal fluid flow in a nonvolcanically active region. The gravity measurement site, SZHK, was located above the fault, and a large gravity difference was detected from March to May 2023, amounting to -47 μGal. The gravity anomaly calculated using the GNSS observed uplift of 18 cm was -10 μGal (Table 2). Nontectonic and tectonic origins to explain this gravity anomaly were considered. Among these anomalies, -2 to -4 μGal was explainable by sea level changes and groundwater fluctuations (Table 4). The subsurface density change caused by coseismic shear slip, which was calculated from dislocation theory, was approximately only -2 μGal. Therefore, we added a vertical tensile fault to represent the fluid flow shown in Fig. 5c. This model produced a change of an additional -4 to -6 μGal with little loss of agreement with the GNSS-observed coseismic displacement field (Cases II–VI in Table 1). Instead of crustal fluid flow, a 40 cm decrease in the groundwater level from March to May 2023 could explain the gravity anomaly of -6 μGal, but evidence is needed to support it. The migrated volume of crustal fluid inferred from our analysis was approximately 10% of the volume that had accumulated on the deeper-dipping fault (Nishimura et al. 2023). The fluid distributions in the shallower regions inferred by seismic tomography might have indirectly supported that the upwelling of fluid due to such large earthquakes has been repeated in the past. In conclusion, this paper provides the first quantitative estimate of the volume of fluid movement associated with the May 2023 earthquake, by combining crustal deformation monitoring with precise gravimetry.

Abbreviations

AMeDAS	Automated Meteorological Data Acquisition System
CMT	Centroid Moment Tensor
CNES	Centre National d'Études Spatiales
GNSS	Global Navigation Satellite System
GSI	Geospatial Information Authority of Japan
IERS	International Earth Rotation Service
JMA	Japan Meteorological Agency

Supplementary Information

The online version contains supplementary material available at https://doi.org/10.1186/s40623-025-02153-5.

Additional file 1.

Acknowledgements

We appreciate the comments of the two anonymous reviewers, which greatly improved the quality of the work. We were able to conduct gravity observations because of the generosity of Suzu city, Wajima city and Noto town. The gravity observations were supported by 2022- and 2023-F2-10 of the Earthquake Research Institute, The University of Tokyo Joint Research program. GWATER-1D software was provided by Dr. Takahito Kazama. We used the earthquake and AMeDAS data provided by the JMA, GNSS data of the Geospatial Information Authority of Japan and the computer systems of the Earthquake and Volcano Information Center of the Earthquake Research Institute, The University of Tokyo. We used the satellite gravity data published by the CNES. Some figures were created using the Generic Mapping Tools (Wessel and Smith 1991).

Author contributions

YT designed the research, analyzed the data and wrote the manuscript. YT, RN, AA, HS, KN and TT carried out gravity observations under the support of TN, YH and AS. TN, YH and AS conducted the GNSS observations. All the authors reviewed the manuscript.

Funding

This study was supported by JSPS KAKENHI grant numbers JP23K17482, JP21H01187, and JP21H05204; JST-Mirai Program (JPMJMI18A1); and the Second Earthquake and Volcano Hazards Observation and Research Program of the Ministry of Education, Culture, Sports, Science and Technology (MEXT) of Japan.

Availability of data and materials

The gravity data reported in this article are available upon reasonable request. The earthquake catalog and AMeDAS data are available at the JMA website (https://www.data.jma.go.jp/svd/eqev/data/daily_map/index.html and https://www.data.jma.go.jp/obd/stats/etrn/index.php, respectively). The GNSS and tide gauge data are available at the GSI website (https://terras.gsi.go.jp/pos_main.php and https://www.gsi.go.jp/kanshi/tide_furnish.html, respectively). The satellite gravity data are available at the CNES website (https://thegraceplotter.com/). The Earth orientation parameters are available at the IERS website (https://datacenter.iers.org/eop.php). The soil data are available at the National Agriculture and Food Research Organization website (https://soil-inventory.rad.naro.go.jp). The first author last accessed these sites in February 2025.

Declarations

Competing interests

The authors declare that they have no competing interests.

Author details

[1]Department of Earth and Planetary Science, The University of Tokyo, Hongo 7-3-1, Bunkyo-Ku, Tokyo 113-0033, Japan. [2]Earthquake Research Institute, The University of Tokyo, Yayoi 1-1-1, Bunkyo-Ku, Tokyo 113-0032, Japan. [3]Present Address: Geospatial Information Authority of Japan, Kitasato 1, Tsukuba, Ibaraki, Japan. [4]Disaster Prevention Research Institute, Kyoto University, Gokasho, Uji, Kyoto, Japan. [5]Institute of Science and Engineering, Kanazawa University, Kakuma-cho, Kanazawa, Ishikawa, Japan.

Received: 14 October 2024 Accepted: 7 February 2025
Published online: 11 March 2025

References

Carter M, Bentley S (1991) Correlations of soil properties. Penetech Press Publishers, London

Crossley D, Hinderer J, Riccardi U (2013) The measurement of surface gravity. Rep Prog Phys 76:046101. https://doi.org/10.1088/0034-4885/76/4/046101

Farrell WE, Clark JA (1976) On postglacial sea level. Geophys J r Astr Soc 46:647–667, https://doi.org/10.1111/j.1365-246X.1976.tb01252.x

Husen S, Kissling E (2001) Postseismic fluid flow after the large subduction earthquake of Antofagasta, Chile. Geology 29:847–850

Ishida T, Mizunoe M, Zongio G, Fuen Y, Higashiyama I (1990) Comparative study of the laboratory methods for measuring soil water diffusivity. Bull Yamagata Univ A Gr Sci 11:97–105, https://yamagata.repo.nii.ac.jp/records/2347 (in Japanese with English abstract)

Kato A (2024) Implications of fault-valve behavior from immediate aftershocks following the 2023 Mj6.5 earthquake beneath the Noto Peninsula, central Japan. Geophys Res Lett 51:e2023GL106444. https://doi.org/10.1029/2023GL106444

Kazama T, Tamura Y, Asari K, Manabe S, Okubo S (2012) Gravity changes associated with variations in local land-water distributions: observations and hydrological modeling at Isawa Fan, northern Japan. Earth Planets Space 64:309–331. https://doi.org/10.5047/eps.2011.11.003

Ma Z, Zeng H, Luo H, Liu Z, Jiang Y, Aoki Y, Wang W, Itoh Y, Lyu M, Cui Y, Yun SH, Hill EM, Wei S (2024) Slow rupture in a fluid-rich fault zone initiated the 2024 Mw 7.5 Noto earthquake. Science 385:866–871. https://doi.org/10.1126/science.ado5143

Matsubara M, Ishiyama T, No T, Uehira K, Mochizuki M, Kanazawa T, Takahashi N, Kamiya S (2022) Seismic velocity structure along the Sea of Japan with large events derived from seismic tomography for whole Japanese Islands including reflection survey data and NIED MOWLAS Hi-net and S-net data. Earth Planets Space 74:171. https://doi.org/10.1186/s40623-022-01724-0

Matsumoto K, Sato T, Takanezawa T, Ooe M (2001) GOTIC2: a program for computation of oceanic tidal loading effect. J Geod Soc Jpn 47:243–248

Mukuhira Y, Uno M, Yoshida K (2022) Slab-derived fluid storage in the crust elucidated by earthquake swarm. Commun Earth Environ 3:286. https://doi.org/10.1038/s43247-022-00610-7

Nakajima J (2022) Crustal structure beneath earthquake swarm in the Noto peninsula, Japan. Earth Planets Space 74:160. https://doi.org/10.1186/s40623-022-01719-x

Nakajima J, Hasegawa A (2007) Subduction of the Philippine Sea plate beneath southwestern Japan: slab geometry and its relationship to arc magmatism. J Geophys Res 112:B08306

Nakamura H, Iwamori H, Kimura J (2008) Geochemical evidence for enhanced fluid flux due to overlapping subducting plates. Nat Geosci 1:380–384

Nishimura T, Hiramatsu Y, Ohta Y (2023) Episodic transient deformation revealed by the analysis of multiple GNSS networks in the Noto Peninsula, central Japan. Sci Rep 13:8381. https://doi.org/10.1038/s41598-023-35459-z

Ohta Y, Ohzono M (2022) Potential for crustal deformation monitoring using a dense cell phone carrier Global Navigation Satellite System network. Earth Planets Space 74:25. https://doi.org/10.1186/s40623-022-01585-7

Okada Y (1985) Surface deformation due to shear and tensile faults in a half-space. Bull Seismol Soc Am 75:1135–1154

Okada T, Savage MK, Sakai S et al (2024) Shear wave splitting and seismic velocity structure in the focal area of the earthquake swarm and their relation with earthquake swarm activity in the Noto Peninsula, central Japan. Earth Planets Space 76:24. https://doi.org/10.1186/s40623-024-01974-0

Okubo S (1992) Gravity and potential changes due to shear and tensile faults in a half-space. J Geophys Res 97:7137–7144. https://doi.org/10.1029/92JB00178
Okubo S (2020) Advances in gravity analyses for studying volcanoes and earthquakes. Proc Japan Acad Ser B 96:50–69. https://doi.org/10.2183/pjab.96.005
Okubo S, Yoshida S, Sato T, Tamura Y, Imanishi Y (1997) Verifying the precision of a new generation absolute gravimeter FG5-Comparison with superconducting gravimeters and detection of oceanic loading tide. Geophys Res Lett 24:489–492
Sato H (1994) The relationship between Late Cenozoic tectonic events and stress field and basin development in northeast Japan. J Geophys Res 99:22261–22274
Sawada A, Hiramatsu Y, Mizubayashi T, Hamada M, Honda R (2012) Geological block structures in the Northern Noto Peninsula, through Gravity Anomalies. Zisin (j Seismol Soc Japan 2nd Ser) 64:235–239. https://doi.org/10.4294/zisin.64.235. (**in Japanese with English abstract**)
Sibson RH (2020) Preparation zones for large crustal earthquakes consequent on fault-valve action. Earth Planets Space 72:31. https://doi.org/10.1186/s40623-020-01153-x
Tamura Y, Sato T, Ooe M, Ishiguro M (1991) A procedure for tidal analysis with a Bayesian information criterion. Geophys J Int 104:507–516
Tanaka Y, Kato A, Sugano T et al (2010) Gravity changes observed between 2004 and 2009 near the Tokai slow-slip area and prospects for detecting fluid flow during future slow-slip events. Earth Planet Space 62:905–913. https://doi.org/10.5047/eps.2010.11.003
Tanaka Y, Suzuki T, Imanishi Y, Okubo S, Zhang X, Ando M, Watanabe A, Saka M, Kato C, Oomori S, Hiraoka Y (2018) Temporal gravity anomalies observed in the Tokai area and a possible relationship with slow slips. Earth Planets Space 70:25. https://doi.org/10.1186/s40623-018-0797-5
Umeda K, Ninomiya A, Negi T (2009) Heat source for an amagmatic hydrothermal system, Noto Peninsula, Central Japan. J Geophys Res 114:B01202
Wessel P, Smith WHF (1991) Free software helps map and display data. EOS Trans AGU 72:445–446
Yamada R, Takahashi T (2021) Temporal and spatial changes of magmatism related to the Japan Sea opening in the Hokuriku region, central Japan. J Geol Soc Jpn 127:507–525 (**in Japanese with English abstract**)
Yoshida S, Seta G, Okubo S, Kobayashi S (1999) Absolute gravity change associated with the March 1997 earthquake swarm in the Izu Peninsula, Japan. Earth Planets Space 51:3–12. https://doi.org/10.1186/BF03352203
Yoshida K, Uchida N, Matsumoto Y, Orimo M, Okada T, Hirahara S et al (2023) Updip fluid flow in the crust of the northeastern Noto Peninsula, Japan, triggered the 2023 Mw 6.2 Suzu earthquake during swarm activity. Geophys Res Lett 50:e2023GL106023. https://doi.org/10.1029/2023GL106023
Yoshimura R, Hiramatsu Y, Goto T (2023) Current Status of 3-D resistivity structure analysis around earthquake swarm region in the Northeastern Noto Peninsula. Rep Coord Comm Earthq Predict 110:476–479, https://cais.gsi.go.jp/YOCHIREN/report/index110.e.html. (in Japanese with English captions)

Publisher's Note

Springer Nature remains neutral with regard to jurisdictional claims in published maps and institutional affiliations.